Observation of multitype topological textures in a subwavelength acoustic Mie resonator

Wan-Na Chen,[1] Hong-Wei Wu,[1,2,3,*] Jing-Yi Lv,[1] Jia-Yu Zheng,[1] Wen-Bing Zhang,[3,†] Nong Zhou,[1] and Zong-Qiang Sheng[1,2]

[1]*School of Mechanics and Photoelectric Physics, Anhui University of Science and Technology, Huainan 232001, China*

[2]*Center for Fundamental Physics, Anhui University of Science and Technology, Huainan 232001, China*

[3]*Institute of Energy, Hefei Comprehensive National Science Center (Anhui Energy Laboratory) Hefei 230031, China*

(Received 24 January 2025; revised 22 April 2025; accepted 24 April 2025; published 9 May 2025)

Topological textures, which refer to nontrivial vector field configurations with topological protection in real space, have aroused great interest in various physical branches. However, conventional topological textures are achieved under stringent excitation conditions that solely hosted a single symmetry configuration in a designed metastructure. Here, we propose a subwavelength acoustic Mie resonator to support localized skyrmion and meron lattice modes for velocity field vectors on structure surface simultaneously depending on the excited location of the point source. We theoretically analyze and numerically calculate the near-field distribution of Mie resonating modes, and find that the higher-order monopole modes correspond to Néel type skyrmion modes, while the multipolar resonating modes belong to meron lattice modes consisting of symmetrically distributed merons and antimerons on the structure surface along the azimuthal direction. We also experimentally observe the near-field distribution of velocity vectors to verify the skyrmions and merons on the structure surface, and the topologically protected property is demonstrated by introducing the structure defects. Multitype topological textures can be simultaneously excited on a subwavelength Mie resonator without strict excitation conditions, which may be a versatile platform for encoding information in versatile topological textures.

DOI: 10.1103/PhysRevB.111.174302

I. INTRODUCTION

Topological textures are a kind of nontrivial vector field distribution in real space, which include vortices [1,2], skyrmions [3,4], merons [5–7], and hopfions [8,9]. With advanced topologically protected property, topological textures hold promise for applications in data storage and information processing in various physical branches. In magnetic materials, skyrmions as a representative topological texture characteristic by skyrmion number have been comprehensively investigated and sprout various derivatives with different vector-field configurations, such as the Néel type [10], Bloch type [11], antitype [12], and so on. Recently, the topological textures have been spread into classical waves, such as electromagnetic waves [13,14], acoustic waves [15–17], elastic waves [18], and water waves [19]. For example, in the electromagnetic wave system, varied topological textures (including skyrmions [3,4], merons [5–7], and hopfions [8,9]) have been constructed in different optical structures for electric/magnetic fields [13,14], spins [20,21], stokes vectors [22,23], and energy flow vectors [24]. In the acoustic wave system, the skyrmions and merons are observed on a designed structure surface for velocity vectors configuration [15,17,25]. Phononic skyrmions form in a hexagonal elastic metaplate for intrinsic spin [18]. Water-wave skyrmion and meron lattices have also been found by linear water-wave interference experiment for the instantaneous displacements of the water-surface particles and the spin density vectors [19]. The topological textures presented in these classical wave systems not only give the opportunity for understanding vector field property, but also provide a platform for manipulating vector fields to process and store classical wave information.

In classical wave systems, the polarization is an inherent property of transverse waves, and provide a natural opportunity to configure the topological textures in electromagnetic and elastic shear waves. Acoustic waves have long been recognized as spinless longitudinal waves. Until recently, theory and experiment on multiple sound beams interference and the acoustic evanescent waves on the structure surface indicate that manipulating the velocity field can induce transverse spin angular moment [26–31]. With a vector property of velocity field, acoustic metasurfaces with hexagonal symmetry are proposed to configure the skyrmion lattice mode for the velocity field. Similarly, an acoustic meron lattice with half of a skyrmion number have also been experimentally observed by designing square metasurfaces [25]. However, the previous observations of acoustic topological textures (including skyrmion and meron lattices) are achieved under the stringent excitation condition that solely hosted a single symmetry configuration in a designed metastructure. A stringent excitation condition means that excitation of lattice-type meron or skyrmion mode requires two or three pairs of loudspeakers, which must be placed relative to each other in order to emit acoustic waves, which interfere with each other to form standing waves so that the meron or skyrmion lattices can be observed on the surface of the structure. To avoid

*Contact author: hwwu@aust.edu.cn

†Contact author: Zhangwb@ie.ah.cn

the strict excitation condition of high symmetry, our previous works [17,32] also demonstrate that a multifrequency localized skyrmionic mode can be supported on subwavelength acoustic metastructures, and by manipulating the skyrmion mode distribution with gradient localized structures. The advantage of the present work over previous work is that we can realize two different topological textures (Néel type skyrmion and meron textures) simultaneously, instead of only the Néel type skyrmion texture [17,32], in a Mie resonance structure by changing the excitation positions. Furthermore, it is worthwhile to expect that multitype topological textures can be freely transformed and coexist in a single metastructures. The realization that diverse topologies can be controlled will open different pathways for encoding information in versatile topological textures.

In this work, we demonstrate that an acoustic Mie resonator with subwavelength scale can support multiple localized skyrmion and meron lattice modes for acoustic velocity field vectors on a structure surface simultaneously, which can be switched by the excited location of point source. We theoretically analyze and numerically calculate the near-field distribution of Mie resonating modes, and find that the higher-order monopole modes correspond to Néel type skyrmion modes, while the multipolar resonating modes belonging to the meron lattice mode consists of a symmetrically distributed meron and antimeron on the structure surface along the azimuthal direction. We also experimentally observe the near-field distribution of velocity vectors to verify the skyrmion and meron lattice modes on the structure surface, and the topologically protected property by introducing the structure defects. These results indicate that multitype topological textures can be simultaneously excited on a Mie resonator without strict excitation conditions, which may be a versatile platform for encoding information in versatile topological textures.

II. THEORETICAL MODEL OF ACOUSTIC MIE RESONATOR

As a start, we first introduce the acoustic Mie resonator with popular zigzag channels to induce the Mie resonating modes and generate acoustic topological textures in acoustic velocity field. As shown in Fig. 1(a), the acoustic Mie resonator is uniformly divided into eight sections with each section having a zigzag channel of total length $L = 528.76$ mm; the height of the structure is $H = 52$ mm with a 2-mm-thick solid bottom and 50-mm-high air columns. A schematic cross-sectional illustration of the acoustic Mie resonator in the x-y plane is depicted in the right image of Fig. 1(a). The inner radius and outer radius are $R_1 = 14$ mm and $R_2 = 65$ mm, respectively, and the thickness of the textured structure corresponding to region II is given by $R_2 - R_1 = 51$ mm. There are eight zigzag channels with length L in the azimuthal direction with opening width $b = 1$ mm, wall thickness $a = 1$ mm, and period length $d = 51.05$ mm. The surrounding media (regions I and III) of the Mie resonator are assumed to be air with density mass ρ_0 and compressive rate β_0, while the channel walls are assumed to be perfect rigid materials.

To analyze the eigenmodes of the Mie resonator, we can treat the zigzag channels with air as straight channels filled

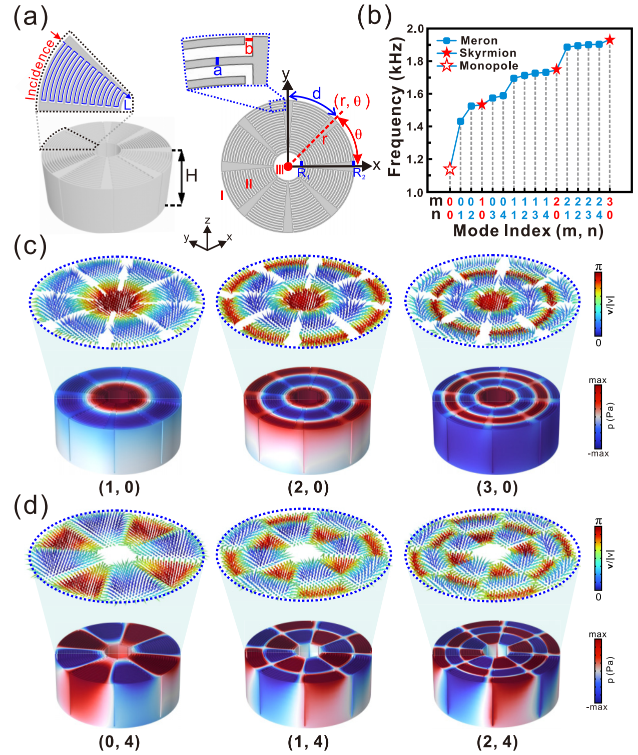

FIG. 1. Schematic structure and simulation results of the skyrmion and meron mode formed by the acoustic velocity field. (a) Left: Three-dimensional structure schematic, where H is the structure height, L represents the total length of a single zigzag channel, and the red arrow is the incidence direction of the sound source. Right: Schematic cross-sectional illustration in the x-y plane, where d is period length, R_1 and R_2 are the inner and outer radii, respectively; The inset shows partial enlargement with opening width b and wall thickness a. (b) The simulation results demonstrate the frequency of the multiple Mie resonating modes as a function of mode index $(m,\ n)$. The blue square represents the meron mode, the red solid pentagram represents the skyrmion mode, and the hollow pentagram represents the monopole mode. (c), (d) Simulation diagram of three different orders of skyrmion modes and multi-pole meron modes, respectively. The direction of the acoustic velocity field is shown by the arrow.

with metafluid, which has efficient compressive rate $\beta' = n_{\mathrm{eff}}\beta_0$ and mass density $\rho' = n_{\mathrm{eff}}\rho_0$, where the effective refractive index is $n_{\mathrm{eff}} = L/(R_2 - R_1)$. Thus, the Mie resonator can be described as eight straight channels with width b periodically inserted into a rigid cylinder along the azimuthal direction with period d. Then, the structure part can be characterized as an acoustic metamaterial with anisotropic effective mass density tensor $\rho_{II} = \mathrm{diag}\,[\rho_{II}^r, \rho_{II}^\theta]$ and scalar compressive rate β_{II} for $R_2 \ll \lambda$ (λ is the working wavelength), which can be expressed as [33,34]

$$\rho_{II}^r = \frac{d}{b}\rho',\quad \rho_{II}^\theta = \infty,\quad \beta_{II} = \frac{b}{d}\beta'. \tag{1}$$

To present the far-field and near-field information of acoustic Mie resonating modes, we can write the pressure and velocity fields in regions I and III as $p_I = \sum_{n=-\infty}^{\infty} A_n H_n^{(1)}(k_0 r)e^{in\theta}$, $v_I =$

$\frac{k_0}{i\omega\rho_0}\sum_{n=-\infty}^{\infty} A_n H_n^{(1)'}(k_0 r)e^{in\theta}$, and $p_{III} = \sum_{n=-\infty}^{\infty} D_n J_n(k_0 r)e^{in\theta}$, $v_{III} = \frac{k_0}{i\omega\rho_0}\sum_{n=-\infty}^{\infty} D_n J_n'(k_0 r)e^{in\theta}$, where A_n and D_n are constants, k_0 and ω are wave number in air and angular frequency, n corresponds to the polar number along the azimuthal direction, $J_n(\cdot)$ and $H_n^{(1)}(\cdot)$ are the first-kind Bessel and Hankel functions. In region II, the pressure and velocity fields can be expressed as

$$p_{II} = \sum_{n=-\infty}^{\infty} [B_n J_0(k_r r) + C_n Y_0(k_r r)]e^{in\theta},$$
$$v_{II} = \frac{k_r}{i\omega\rho_{II}^r}\sum_{n=-\infty}^{\infty} [B_n J_1(k_r r) + C_n Y_1(k_r r)]e^{in\theta}, \tag{2}$$

where $k_r = n_{\text{eff}}k_0$. B_n and C_n are also undetermined coefficients. For $H \ll \lambda$, we can obtain the resonating condition for the individual modes with a given n in the x-y plane by applying matching boundary conditions on p and v at $r = R_1$ and $r = R_2$; the transcendental equation is

$$bq_1 H_n^{(1)}(k_0 R_2) + dq_2 H_n^{(1)'}(k_0 R_2) = 0, \tag{3}$$

where $q_1 = J_1(k_r R_2) - \delta Y_1(k_r R_2)$, $q_2 = J_0(k_r R_2) - \delta Y_0(k_r R_2)$, and $\delta = [bJ_1(k_r R_1)J_n(k_0 R_1) + dJ_0(k_r R_1)J_n'(k_0 R_1)]/[bY_1(k_r R_1)J_n(k_0 R_1) + dY_0(k_r R_1)J_n'(k_0 R_1)]$. The far-field scattering cross section can be expressed as

$$\sigma_{\text{sc}} = \frac{4c}{\omega}\sum_{n=-\infty}^{\infty} |a_n|^2, \tag{4}$$

where $a_n = -i^n[bq_1 J_n(k_0 R_2) + dq_2 J_n'(k_0 R_2)]/[bq_1 H_n^{(1)}(k_0 R_2) + dq_2 H_n^{(1)'}(k_0 R_2)]$.

To check the above theoretical analysis, we also calculate the eigenmodes of the designed acoustic Mie resonator by full-wave simulation based on the pressure acoustic model of the simulation software COMSOL Multiphysics, and get the relationship between eigenfrequency and mode index as shown in Fig. 1(b). The mode index $(m,\ n)$ is used to distinguish different Mie resonating modes, where $m = 0, 1, 2,...$ represents the order number along the radial direction, and $n = 0, 1, 2,...$ represents the polar number along the azimuthal direction, such as monopole, dipole, quadrupole, and so on. The multiorder multipolar meron modes occur when $n \neq 0$, which has been represented by a blue square. When $n = 0$, there are resonating modes marked with the solid pentagrams that represent the higher-order monopolar modes and the hollow pentagram represents the lowest-order monopole mode. Figure 1(c) shows the acoustic pressure and velocity distributions of the higher-order monopolar modes with three different orders m, including (1, 0), (2, 0), and (3, 0). The order number m describes the flipped number of velocity vectors along the radial direction. As can be seen from the flip of the vector arrows, this is consistent with a Néel-type skyrmion distribution. To demonstrate the skyrmion configuration of velocity vector distribution for higher-order monopolar modes, we calculate the skyrmion number by [14,17]

$$s = \frac{1}{4\pi}\iint \vec{n}\cdot\left(\frac{\partial\vec{n}}{\partial x}\times\frac{\partial\vec{n}}{\partial y}\right)dxdy, \tag{5}$$

In our model, the acoustic skyrmion number can reflect the topology of a skyrmionic configuration by the velocity field distributions according to Eq. (5), where $\vec{n} = \text{Re}(\vec{v})/|\text{Re}(\vec{v})|$. Based on the mapping from the three-dimensional (3D) parametrized sphere to the two-dimensional (2D) vector field by longitude $\Phi(\theta)$ and latitude $\Gamma(r)$, the skymion number can be separated into additional topological numbers:

$$s = \left(\frac{1}{2}\int_{r_1}^{r_2}\sin\Gamma(r)dr\right)\left(\frac{1}{2\pi}\int_0^{2\pi}\frac{d\Phi(\theta)}{d\theta}d\theta\right) = P\cdot M, \tag{6}$$

where the integer $P = -\frac{1}{2}[\cos\Gamma(r)]|_{r=r_1}^{r=r_2}$ defines the polarity and the integer $M = \frac{1}{2\pi}[\Phi(\theta)]|_0^{2\pi}$ defines the vorticity. In this work, for Néel-type skyrmion mode (1, 0), its vorticity $M = 1$, and the polarity $P = -1$ in this domain of integration $r_1 = 0,\ r_2 = R_2$, thus the skyrmion number is calculated as $s = -1$. We find that the skyrmion numbers s of resonating modes with indexes (1, 0), (2, 0), and (3, 0) calculated from numerical simulation correspond to $s = -1.035$, 0.012, and -1.016, which are close to the theoretical value of -1, 0, and -1, respectively. It is worthwhile to note that the upward reference vector of Eq. (6) localizes at the structure center for skyrmion modes, while it locates at region II for meron modes for calculating the skyrmion numbers. The result indicates that the higher-order monopolar mode belongs to localized Néel-type skyrmionic modes [17]. The blank regions in the velocity field distribution of Fig. 1(c) correspond to negligible velocity magnitude on the hard walls. Particularly, the velocity vector of the lowest-order monopolar mode with mode index (0, 0) does not have the vector flipped process from structure center to edge as shown in Fig. S1 of the Supplemental Material [35], thus it is not a skyrmionic mode.

Furthermore, we also present the multipolar ($n > 0$) Mie resonating modes in Fig. 1(d), and other multipolar mode distributions are shown in Fig. S2 of the Supplemental Material [35]. It is well known that the subwavelength cylinder Mie resonating structure naturally provides the interference between clockwise and anticlockwise propagating waves along the azimuthal direction to the formed standing wave, and the acoustic field will also be confined by the structure's inner and outside boundaries along the radial direction, as can be seen in Eq. (2). Thus, the multipolar ($n > 0$) Mie resonating modes can be recognized as the meron lattice mode distributed on the structure surface similar to the case of the acoustic square metastructure [25] with two pairs of bound boundaries. It is obvious that the Mie resonating structure with eight channels will support a perfect meron lattice for the Mie resonating mode with indices (0, 4), (1, 4), (2, 4), thus we present them in Fig. 1(d); other multipolar resonating modes are also meron lattice with rough velocity field distribution due to the limitation of eight channels. As shown in Figs. 1(d) and S2, the meron lattices consisting of the meron and antimeron modes formed by the acoustic velocity field are symmetrically distributed on the structure surface. The colors assigned to the structure indicate the distribution of sound pressure fields, while the color vectors above the structure represent the configuration of velocity fields. To verify the above description, we also calculate the skyrmion numbers of the meron and antimeron in mode (0, 4); the numerical results correspond

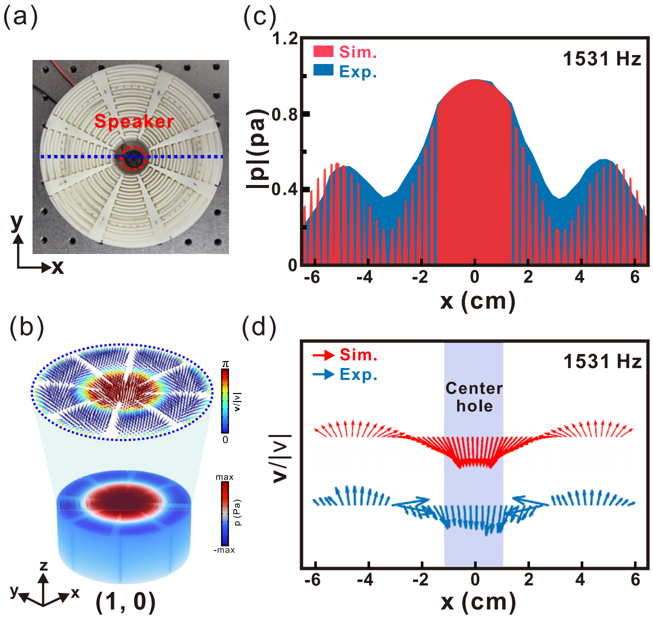

FIG. 2. Acoustic skyrmion simulation and experimental measurement of sound pressure distribution and velocity field distribution. (a) Schematic diagram of the experimental setup. (b) Simulation diagram of structural sound pressure field distribution and the (1, 0) skyrmion mode formed by the acoustic velocity field. (c) The simulated (red) and experimentally measured (blue) sound pressure fields are distributed on the sample surface. (d) The acoustic velocity field distribution of the simulated (red arrows) and experimental (blue arrows) is illustrated, along the blue dotted line of (a). The simulation and experiment work frequency are both 1531 Hz.

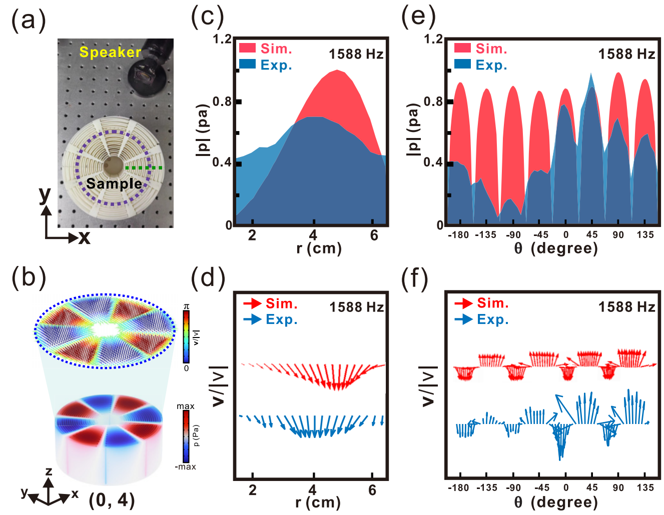

FIG. 3. Acoustic meron simulation and experimental measurement of sound pressure distribution and velocity field distribution. (a) Schematic diagram of the experimental setup. The green and purple dotted lines indicate measurement directions in radial and azimuthal direction, respectively. (b) Simulation diagram of structural sound pressure field distribution and the (0, 4) meron mode formed by the acoustic velocity field. (c), (e) The simulated (red) and experimentally measured (blue) sound pressure fields are distributed on the sample surface in radial and azimuthal direction, respectively. (d), (f) The distributions of the simulated (red arrows) and experimental (blue arrows) velocity fields in radial and azimuthal direction, respectively. The simulation and experiment work frequency are both 1588 Hz.

to $s = 0.491$ and -0.516, which are close to the theoretical values of 0.5 and -0.5, respectively.

III. NEAR-FIELD MEASUREMENT OF TOPOLOGICAL TEXTURES

Above, we have theoretically analyzed and numerically calculated the eigenmodes of the Mie resonating structure with subwavelength scale, and find that the structure can support localized skyrmion and meron lattice, simultaneously. These results indicate that multitype topological textures can be simultaneously excited on a Mie resonator without strict excitation conditions. Next, we will observe the topological textures of the acoustic Mie resonator in experiment. A photograph of the acoustic Mie resonator sample with resin material by means of 3D printing is shown in Fig. 2(a), where the loudspeaker is placed in the center of the sample to excite the (1, 0) skyrmion mode. If the (1, 0) skyrmion mode is excited at the edge of the structure, it will be suppressed by the neighboring (0, 2) quadrupole mode that has a better local effect [see Fig. S2(a) in the Supplemental Material for details], so we excite the (1, 0) skyrmion mode in the center of the structure by means of structure symmetry to suppress the quadrupole mode. Figure 2(b) depicts the distribution of the acoustic pressure field and velocity field of the (1, 0) skyrmion mode by numerical calculation. It can be observed that the direction of the velocity vector is downward at the center, while the vector direction keeps flipping as the radius increases, eventually going upward at the edge of the Mie resonator.

During the experiment, the sine wave signal is generated by the signal generator (AFG1022, Tektronix), amplified in the power amplifier (CPA2400, SinoCinetech), and passed through a splitter box (FM02-12D, Tatsukawa) to drive the speaker. We use a free-field microphone (MPA416, BSWA TECH) to measure the sound pressure above the surface of the sample along the blue dotted line of Fig. 2(a), and record the sound pressure intensity. We first measure the sound pressure by placing the microphone close to the surface of the structure, and then measure the sound pressure again by raising the microphone to a certain distance to obtain the sound pressure measurement results at different heights. The measured and simulated sound pressure distributions at 1531 Hz are shown in Fig. 2(c), and the magnitude and direction of the corresponding sound velocity fields using measured sound pressure field distributions are given by $\vec{v} = \frac{1}{i\omega\rho_0}\nabla p$, where ω and ρ_0 are the angular frequency and mass density of air, respectively. The simulated and experimental results of sound velocity field distribution along the diameter on the sample surface are shown in Fig. 2(d), and the area of center hole at sample has been marked with light purple. We can find that the experimental result (blue arrows) agrees well with the simulated result (red arrows).

Next, we also experimentally observe the (0, 4) meron lattice mode of the acoustic velocity field. Figure 3(a) schematically shows the experimental setup, where the speaker is placed at a distance of 5 cm from the edge of the structure and aligned with the opening of the zigzag grooves. The numerical simulation result of the (0, 4) meron lattice mode is depicted in Fig. 3(b), which includes the distribution of sound pressure and velocity field. It can be seen that each of the eight zigzag channels produces a meron pattern, alternating positive and negative, which together form a meron lattice mode.

We measure the sound pressure field data along the purple and green dotted lines of Fig. 3(a) on the surface of the structure, and then process the measured data to obtain the sound velocity field distribution. In the radial direction, the trend of the measured sound pressure values (blue) is generally consistent with that of the simulation (red) as shown in Fig. 3(c), and the corresponding velocity vectors (blue arrows) match well with that of the simulation (red arrows) in Fig. 3(d). In addition, along the azimuthal direction, the measured sound pressure shows a peak at each section of the structure in Fig. 3(e), and some of the peaks are not obvious because, compared to the larger peaks, these smaller peaks are suppressed and appear to have a less pronounced trend. Figure 3(f) demonstrates that the measured azimuthal velocity vectors are in general agreement with the simulated velocity field distribution.

IV. ROBUSTNESS MEASUREMENT OF TOPOLOGICAL TEXTURES

It is well known that the topological textures are protected in real space against to structure defects and disorders. Thus, we experimentally observe the robustness of the (1, 0) skyrmion mode and the (0, 4) meron lattice mode in acoustic velocity field, and verify that those topological textures have a high level of robustness against structural defects. We intentionally introduced defects in the symmetric structures by inserting rigid materials to block the channels as shown in the black region of Fig. 4(a). We simulate and obtain the acoustic pressure field and velocity field distributions of the (1, 0) skyrmion mode based on the simulation software COMSOL Multiphysics, as shown in Fig. 4(b). We find that the sound pressure field distribution is somewhat distorted, but the acoustic velocity field maintains the skyrmionic configuration.

Next, we measure the magnitude of the sound pressure field on the surface of the sample along the blue dotted line of Fig. 4(a). The experimental results demonstrate that the defects diminish acoustic pressure intensity in the corresponding local area, but the overall trend of sound pressure can still be maintained well, as shown in Fig. 4(c). The magnitude and direction of the corresponding sound velocity fields are determined based on measured sound pressure field distribution. As depicted in Fig. 4(d), the sound velocity field (red arrows) is locally perturbed at the location of the defects, compared to the velocity field without defects (black arrows), but the skyrmion distribution is still retained. In order to minimize the effect of the presence of structural defects that cause perturbations in the near-field sound intensity around the defects, the microphone will be raised so that the sound pressure can be measured at a greater height difference for obtaining the accurate direction of velocity fields. Moreover, the experimentally measured skyrmion mode (blue arrows)

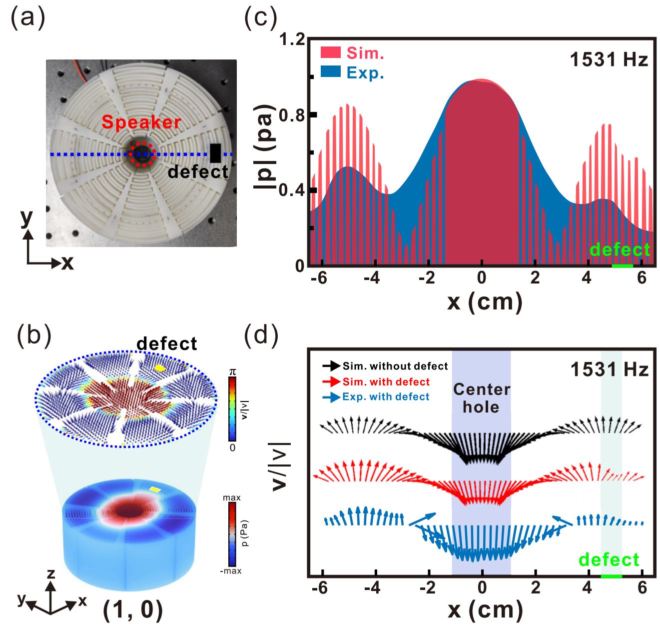

FIG. 4. Robustness experiment of the (1, 0) skyrmion mode. (a) Schematic diagram of the robustness experiment setup. The black zone shows the location of the defect in the sample. (b) Simulation diagram of the (1, 0) skyrmion mode formed by the acoustic velocity field. The yellow zones show the location of the defect in sound pressure field and velocity field, respectively. (c) The simulated and experimentally measured sound pressure fields are distributed on the sample surface. (d) The velocity field distribution without defects (black arrows), the simulated (red arrows) and experimental (blue arrows) results of sound velocity field distribution with defects, along the blue dotted line in (a). The simulation and experiment work frequency are both 1531 Hz.

of the velocity field is quite consistent with the simulation results (red arrows), which confirms the remarkable structural stability inherent to the (1, 0) skyrmion configuration under defects.

Similarly, we experimentally observe the robustness of the (0, 4) meron mode in the acoustic velocity field. Figure 5(a) schematically shows the experimental setup, where the defect is located at the black area, and the speaker is placed at a distance of 5 cm from the edge of the structure and aligned with the opening of the zigzag grooves. The numerical simulation result of the (0, 4) meron mode under defect is depicted in Fig. 5(b), and the white areas are where the defects are located in the sound pressure field and velocity field, respectively. The working frequency of both simulation and experiment is 1588 Hz. It is obvious that the sound pressure field and velocity field hold the meron lattice mode well, indicating a high level of robustness against structural defects.

We measure the sound pressure field data along the orange, green, and purple dotted lines of Fig. 5(a) on the surface of the structure, and then process the measured data and draw it in vector form. Figures 5(c) and 5(e) show that the simulated and experimentally measured sound pressure fields are distributed on the sample surface in radial (green dotted line) and azimuthal (purple dotted line) directions, respectively. The experimental results of the acoustic velocity distribu-

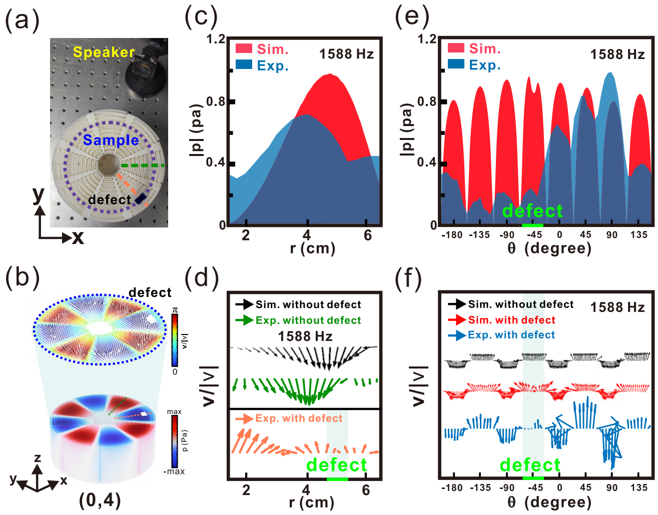

FIG. 5. Robustness experiment of the (0, 4) meron mode. (a) Schematic diagram of the experimental setup. The green, orange and purple dotted lines indicate different measurement directions. The black area shows the location of the defect in the sample. (b) Simulation diagram of the (0, 4) meron mode formed by the acoustic velocity field. The white areas show the location of the defect in the sound pressure field and velocity field, respectively. (c), (e) The simulated and experimentally measured sound pressure fields are distributed on the sample surface in radial (the green dotted line) and azimuthal (the purple dotted line) directions, respectively. (d) Experimental measurements of the meron mode in the radial direction. Green (orange) arrows represent experimental measurements of the sound velocity field without (with) defect. (f) Experimental measurements of the meron mode in the azimuthal direction. The green band is the area where the defect is located.

tions in the radial direction are shown in Fig. 5(d); it can be observed that the orange arrows indicate that the acoustic velocity field has been destroyed under defects, however, the acoustic velocity distributions in the neighboring regions (the green arrows) remain good. This is because the defect destroys the localized meron distribution in that region, while the meron distributions in other regions are maintained. This can be further verified from the experimental measurement result of the (0, 4) meron mode along the azimuthal direction. Figure 5(f) shows that the sound velocity field in the region where the defect is located (-45°) is destroyed, while the meron distributions in the other directions are well maintained. This indicates that the (0, 4) mode has the robust property of local destruction but global topology.

V. CONCLUSION

In conclusion, we design an acoustic Mie resonator with subwavelength scale supporting multiple skyrmion and meron lattice modes in velocity field on the surface of the structure simultaneously, excited by different locations of the point source. Based on the near-field distribution of Mie resonating modes, we find that the higher-order monopole modes correspond to Néel type skyrmion modes, while the multipolar resonating modes belong to the meron lattice mode consisting of symmetrically distributed meron and antimeron structure surface along the azimuthal direction. Moreover, we experimentally observe the topological textures of skyrmion and meron lattices in the velocity field on the surface of the structure, and verify the topologically protective property of the Mie resonator against defects. The Mie resonator can generate multitype topological textures simultaneously without strict excitation conditions, which may open a different avenue in storing data and encoding information of acoustic waves.

ACKNOWLEDGMENTS

This work was supported by scientific research projects of colleges and universities in Anhui Province (Grant No. 2022AH040114) and the University Synergy Innovation Program of Anhui Province (Grant No. GXXT-2022-015). W.-N.C. thanks for the support of Anhui University of Science and Technology of Graduate Student Innovation Fund Program (Grant No. 2024cx2122).

DATA AVAILABILITY

The data that support the findings of this article are openly available [36]; embargo periods may apply.

[1] L. Xiong, Y. T. Li, D. Halbertal, M. Sammon, Z. Y. Sun, S. Liu, J. H. Edgar, T. Low, M. M. Fogler, C. R. Dean, A. J. Millis, and D. N. Basov, Polaritonic vortices with a half-integer charge, Nano Lett. **21**, 9256 (2021).
[2] J. Iwasaki, M. Mochizuki, and N. Nagaosa, Current-induced skyrmion dynamics in constricted geometries, Nat. Nanotechnol. **8**, 742 (2013).
[3] X. R. Lei, A. P. Yang, P. Shi, Z. W. Xie, L. P. Du, A. V. Zayats, and X. C. Yuan, Photonic spin lattices: Symmetry constraints for skyrmion and meron topologies, Phys. Rev. Lett. **127**, 237403 (2021).
[4] Y. Tokura and N. Kanazawa, Magnetic skyrmion materials, Chem. Rev. **121**, 2857 (2020).
[5] A. Ghosh, S. Yang, Y. Dai, Z. K. Zhou, T. Y. Wang, C. B. Huang, and H. Petek, A topological lattice of plasmonic merons, Appl. Phys. Rev. **8**, 041413 (2021).
[6] C. F. Lu, B. Wang, X. Fang, D. P. Tsai, W. M. Zhu, Q. H. Song, X. Deng, T. He, X. Y. Gong, H. Luo, Z. S. Wang, X. H. Dai, Y. Z. Shi, and X. B. Cheng, Nanoparticle deep-subwavelength dynamics empowered by optical meron-antimeron topology, Nano Lett. **24**, 104 (2024).
[7] M. Król, H. Sigurdsson, K. Rechcińska, P. Oliwa, K. Tyszka, W. Bardyszewski, A. Opala, M. Matuszewski, P. Morawiak, R. Mazur, W. Piecek, P. Kula, P. G. Lagoudakis, B. Piętka, and J. Szczytko, Observation of second-order meron polarization textures in optical microcavities, Optica **8**, 255 (2021).
[8] H. W. Wang and S. H. Fan, Photonic spin hopfions and monopole loops, Phys. Rev. Lett. **131**, 263801 (2023).

[9] X. S. Wang, A. Qaiumzadeh, and A. Brataas, Current-driven dynamics of magnetic hopfions, Phys. Rev. Lett. **123**, 147203 (2019).

[10] I. Kézsmárki, S. Bordács, P. Milde, E. Neuber, L. M. Eng, J. S. White, H. M. Rønnow, C. D. Dewhurst, M. Mochizuki, K. Yanai, H. Nakamura, D. Ehlers, V. Tsurkan, and A. Loidl, Néel-type skyrmion lattice with confined orientation in the polar magnetic semiconductor GaV_4S_8, Nat. Mater. **14**, 1116 (2015).

[11] J. Jena, B. Göbel, T. P. Ma, V. Kumar, R. Saha, I. Mertig, C. Felser, and S. S. P. Parkin, Elliptical Bloch skyrmion chiral twins in an antiskyrmion system, Nat. Commun. **11**, 1115 (2020).

[12] A. K. Nayak, V. Kumar, T. P. Ma, P. Werner, E. Pippel, R. Sahoo, F. Damay, U. K. Rößler, C. Felser, and S. S. P. Parkin, Magnetic antiskyrmions above room temperature in tetragonal Heusler materials, Nature (London) **548**, 561 (2017).

[13] S. Tsesses, E. Ostrovsky, K. Cohen, B. Gjonaj, N. H. Lindner, and G. Bartal, Optical skyrmion lattice in evanescent electromagnetic fields, Science **361**, 993 (2018).

[14] Y. J. Shen, Q. Zhang, P. Shi, L. P. Du, X. C. Yuan, and A. V. Zayats, Optical skyrmions and other topological quasiparticles of light, Nat. Photonics **18**, 15 (2023).

[15] H. Ge, X.-Y. Xu, L. Liu, R. Xu, Z.-K. Lin, S.-Y. Yu, M. Bao, J.-H. Jiang, M.-H. Lu, and Y.-F. Chen, Observation of acoustic skyrmions, Phys. Rev. Lett. **127**, 144502 (2021).

[16] R. D. Muelas-Hurtado, K. Volke-Sepúlveda, J. L. Ealo, F. Nori, M. A. Alonso, K. Y. Bliokh, and E. Brasselet, Observation of polarization singularities and topological textures in sound waves, Phys. Rev. Lett. **129**, 204301 (2022).

[17] P. Hu, H. W. Wu, W. J. Sun, N. Zhou, X. Chen, Y. Q. Yang, and Z. Q. Sheng, Observation of localized acoustic skyrmions, Appl. Phys. Lett. **122**, 022201 (2023).

[18] L. Y. Cao, S. Wan, Y. Zeng, Y. F. Zhu, and B. Assouar, Observation of phononic skyrmions based on hybrid spin of elastic waves, Sci. Adv. **9**, eadf3652 (2023).

[19] D. A. Smirnova, F. Nori, and K. Y. Bliokh, Water-wave vortices and skyrmions, Phys. Rev. Lett. **132**, 054003 (2024).

[20] Q. Zhang, Z. W. Xie, L. P. Du, P. Shi, and X. C. Yuan, Bloch-type photonic skyrmions in optical chiral multilayers, Phys. Rev. Res. **3**, 023109 (2021).

[21] Q. Zhang, Z. W. Xie, P. Shi, H. Yang, H. R. He, L. P. Du, and X. C. Yuan, Optical topological lattices of Bloch-type skyrmion and meron topologies, Photonics Res. **10**, 947 (2022).

[22] R. Tamura, P. Kumar, A. S. Rao, K. Tsuda, F. Getzlaff, K. Miyamoto, N. M. Litchinitser, and T. Omatsu, Direct imprint of optical skyrmions in azopolymers as photoinduced relief structures, APL Photonics **9**, 046104 (2024).

[23] S. Cao, L. P. Du, P. Shi, and X. C. Yuan, Topological state transitions of skyrmionic beams under focusing configurations, Opt. Express **32**, 4167 (2024).

[24] S. Wang, Z. Zhou, Z. Zheng, J. Sun, H. Cao, S. Song, Z. L. Deng, F. Qin, Y. Cao, and X. Li, Topological structures of energy flow: Poynting vector skyrmions, Phys. Rev. Lett. **133**, 073802 (2024).

[25] N. Zhou, W. N. Chen, W. J. Sun, Z. Q. Sheng, and H. W. Wu, Observation of acoustic meron textures, Appl. Phys. Lett. **125**, 042204 (2024).

[26] C. Z. Shi, R. K. Zhao, Y. Long, S. Yang, Y. Wang, H. Chen, J. Ren, and X. Zhang, Observation of acoustic spin, Nat. Sci. Rev. **6**, 707 (2019).

[27] L. Burns, K. Y. Bliokh, F. Nori, and J. Dressel, Acoustic versus electromagnetic field theory: Scalar, vector, spinor representations and the emergence of acoustic spin, New J. Phys. **22**, 053050 (2020).

[28] Y. Long, D. M. Zhang, C. W. Yang, J. M. Ge, H. Chen, and J. Ren, Realization of acoustic spin transport in metasurface waveguides, Nat. Commun. **11**, 4716 (2020).

[29] K. Y. Bliokh and F. Nori, Transverse spin and surface waves in acoustic metamaterials, Phys. Rev. B **99**, 020301(R) (2019).

[30] K. Y. Bliokh and F. Nori, Spin and orbital angular momenta of acoustic beams, Phys. Rev. B **99**, 174310 (2019).

[31] Y. Long, C. W. Yang, H. Chen, and J. Ren, Universal geometric relations of acoustic spin, energy flux, and reactive power, Phys. Rev. Appl. **19**, 064053 (2023).

[32] W. J. Sun, H. W. Wu, P. Hu, N. Zhou, X. Chen, Y. Q. Yang, and Z. Q. Sheng, Localized manipulation of spoof surface acoustic skyrmions with deep-subwavelength gradient structures, Appl. Phys. Lett. **122**, 202201 (2023).

[33] H. W. Wu, W. Li, S. L. Cheng, Y. Q. Yin, and Z. Q. Sheng, Acoustic generalized Kerker effect, Appl. Phys. Express **14**, 095501 (2021).

[34] X. Zhu, B. Liang, W. Kan, Y. Peng, and J. Cheng, Deep-subwavelength-scale directional sensing based on highly localized dipolar Mie resonances, Phys. Rev. Appl. **5**, 054015 (2016).

[35] See Supplemental Material at http://link.aps.org/supplemental/10.1103/PhysRevB.111.174302 for brief description on the scattering properties of the acoustic Mie resonator.

[36] The data of figures in main text can be obtained at https://pan.baidu.com/s/10r6DvRvRgZWx_fMQjoV6aQ?pwd=f49w.